Materials and Solidification http://mc03.manuscriptcentral.com/msolid
Materials and Solidification 2026, **2**: 9580025
https://doi.org/10.26599/MAS.2026.9580025
Review

Electrides for electronic devices: From demonstrated applications to emerging concepts

Chenyang Zhao[1], Kang Chen[2], Qingyu Meng[2], Yelizaveta A. Morkhova[3, 4, 5], Yutong Gong[3, 4, 6], Zhiqi Wang[3, 4, 6, ✉]

[1] *School of Telecommunications Engineering, Xidian University, Xi'an 710072, China.*

[2] *Shaanxi Yanchang Petroleum Energy Supplier Co., LTD, Xi'an 710049, China.*

[3] *State Key Laboratory of Solidification Processing, School of Materials Science and Engineering, Northwestern Polytechnical University, Xi'an 710072, China.*

[4] *Xi'an Key Laboratory of Intelligent Design of Energy Catalytic Materials, Northwestern Polytechnical University, Xi'an 710072, China.*

[5] *Samara Center for Theoretical Materials Science (SCTMS), Samara State Technical University, Samara 443100, Russia.*

[6] *Research & Development Institute of Northwestern Polytechnical University in Shenzhen, Shenzhen 518057, China.*

✉ Corresponding author.

E-mail: wangzhiqi@mail.nwpu.edu.cn

Received: October 31, 2026; Revised: November 7, 2026; Accepted: November 9, 2026

© Author(s) 2025.

Abstract: An electride is a compound in which electrons confined within crystallographic voids act as anions. Interest in electrides has grown steadily since the discovery of room-temperature-stable $[Ca_{24}Al_{28}O_{64}]^{4+}(4e^-)$ (C12A7:e^-) in 2003, although subsequent research has focused predominantly on heterogeneous catalysis. This mini-review shifts the focus to electronic and optoelectronic devices, critically examining which applications have been experimentally demonstrated, how their performance compares with that of established technologies, and why many theoretically proposed devices remain unrealized. Vacuum and plasma electron sources represent the most mature application domain. Heaterless hollow cathodes incorporating C12A7:e^- inserts can ignite at room temperature and operate continuously for more than 950 h, while plasma-activated C12A7:e^- converter grids increase the extracted negative hydrogen ion (H^-) beam current by 70% without the use of cesium. Thin-film optoelectronics constitute a second experimentally validated domain: a 4 nm amorphous C12A7:e^- electron-injection layer deposited by room-temperature sputtering reduces the turn-on voltage of an inverted organic light-emitting diode from 9.2 to 4.7 V. In contrast, barrier-free Ohmic contacts to two-dimensional semiconductors, spintronic injectors, and devices based on topological electrides remain largely at the computational proposal stage. By comparing experimentally measured device figures of merit with relevant materials benchmarks, this review also examines from an apparent field-emission barrier of 0.6 eV to a surface work function near 5.0 eV for a single compound and discusses the factors underlying this apparent disparity. We argue that the principal obstacle to broader device integration is not a lack of promising intrinsic electronic properties, but the chemical instability of many electrides under device-processing and operating conditions. Accordingly, future efforts should pursue two complementary directions: process optimization, contact engineering, and reliability assessment for electrides already demonstrated in functional devices; and the targeted discovery and integration of chemically robust electrides for applications inaccessible to more reactive compounds.

Keywords: Electride; Work function; Electron emission; Hollow cathode; Electron-injection layer; Ohmic contact

1. Introduction

An electride is a crystalline or amorphous compound in which interstitial electrons act as anions [1-2]. The cations form a structural framework, and the charge-balancing electrons are confined within its voids, such as cages, channels, or interlayer galleries. Rather than occupying atomic orbitals or a conventional conduction band, these electrons function as discrete anionic species. Organic electrides crystallized with crown ethers and cryptands were obtained in the 1980s [3], but they decomposed well below room temperature, which kept the subject inside physical chemistry. That changed in 2003, when Hideo Hosono and co-workers removed the extra-framework oxygen from the mineral mayenite and obtained $[Ca_{24}Al_{28}O_{64}]^{4+}(4e^{-})$, conventionally written C12A7:e^{-}: an inorganic electride that is stable, conductive and handleable at room temperature [4-5].

For device engineers, the defining attraction of an inorganic electride is a property decoupling that does not exist in conventional elemental metals. In a simple metal, a low work function (φ) comes bundled with severe chemical reactivity, because the same loosely bound valence electrons that escape the surface easily also reduce oxygen and water rapidly. This thermodynamic coupling explains why caezium, barium, and calcium surfaces require ultrahigh vacuum, getters, or heated dispenser reservoirs, and why the compromise LiF/Al bilayer cathode has persisted in commercial organic light-emitting diodes (OLEDs). In an electride, by contrast, the loosely bound electrons reside within the cavities of a refractory oxide, nitride, carbide, chalcogenide, or intermetallic silicide lattice: the cationic framework supplies mechanical, thermal, and chemical robustness, while the anionic electrons supply the low work function. C12A7:e^{-} is the classic oxide example. Derived from a calcium aluminate constituent of aluminous cement, it exhibits a clean-surface work function of 2.4 eV—

comparable to metallic potassium—yet is sufficiently robust to be machined, polished, and stored in ambient air [6-7].

Despite this promise, the electride literature has grown asymmetrically. Ammonia synthesis and related heterogeneous catalysis dominate published output [6], because electrides act as potent electron donors and reversible hydride hosts when supporting transition-metal nanoparticles. High-throughput computational screening has simultaneously expanded the catalogue of candidate compounds far beyond what experimentalists synthesise routinely: database searches have identified dozens of two-dimensional (2D) layered candidates [8-9], a systematic screen across more than 60 000 Materials Project entries returned 65 previously unrecognised electrides [10], and recent high-throughput and machine-learning studies have further expanded the pool to 3D topological electrides [11] and ternary intermetallic A_2BC_2 electrides [12-13]. By contrast, the number of electride-based electronic devices with measured hardware figures of merit remains of order tens rather than thousands. While this gap is often framed as a technology-transfer delay between theoretical prediction and device fabrication, it reflects a deeper targeting mismatch. Most computational screens for electronic applications rank candidates solely on interstitial electron localisation and vacuum work function, rarely evaluating chemical durability in air, moisture, or lithographic solvents—the exact criteria that determine whether a compound can survive practical device processing.

This mini-review critically evaluates electrides that have been experimentally demonstrated in, or theoretically proposed for, electronic and optoelectronic devices. Section 2 surveys the materials landscape, comparing oxide, layered nitride/carbide, self-passivating chalcogenide, and intrinsically stable intermetallic electrides, and examines the origins of the wide variation in reported work functions. Sections 3-6 review device applications in descending order of experimental maturity: vacuum and plasma electron sources (Section 3), charge-injection interlayers in organic and thin-film optoelectronics (Section 4), interconnects and Ohmic contacts in two-dimensional nanoelectronics (Section 5), and emerging concepts in resistive memory, spintronics, and superconductivity (Section

6). Section 7 synthesizes the cross-cutting challenges of device integration and identifies two complementary strategies for mitigating ambient degradation: stabilizing the intermetallic framework intrinsically and exploiting kinetic surface self-passivation. Building on these insights, Section 8 presents a dual-track roadmap that combines process engineering for electrides already demonstrated in functional devices with device-level exploration of chemically robust intermetallic and self-passivating electrides.

Existing reviews focus on catalysis, single-compound processing, or magnetic electrides [6-7, 11, 14-15]. Our article takes a different angle. We assess each application at the device level and grade the supporting evidence. Applications fall into three tiers: working hardware, materials-level data, or theoretical prediction. Each is benchmarked against the incumbent technology under stated operating conditions.

This review instead grades each application by its level of evidence and compares it with the incumbent technology. Two points emerge from that comparison. First, the unrealized devices are not limited by their predicted performance. Every application already built in hardware uses C12A7:e^-, which tolerates air. Most proposed applications use 2D electrides, whose interlayer electrons are consumed during lithography (Section 5.1). The gap is therefore one of chemical stability under processing, not of intrinsic electronic quality. Second, this changes what a screening criterion should be. Ranking candidates by work function alone is not sufficient. Two families meet the stability requirement, the self-passivating chalcogenides and the intrinsically stable intermetallic compounds, and they are not interchangeable. A native oxide skin blocks low-bias injection, so intermetallic electrides are the better choice for contacts and emitters (Section 7.1). Sections 7 and 8 develop this argument into a research agenda.

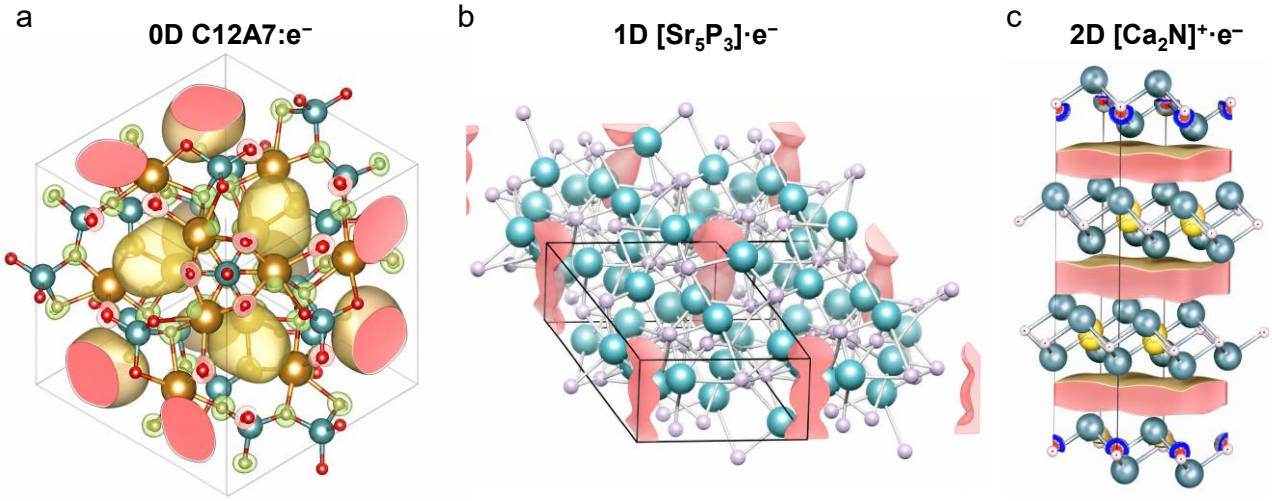
Throughout the review, we explicitly distinguish three levels of evidence: (i) functional devices with measured electrical or beam-level performance, (ii) materials-level measurements from which

potential device utility is inferred, and (iii) first-principles predictions that have yet to be experimentally validated.

2. Materials Platform: Dimensionality, Work Function, and Processing

2.1 Anionic Electron Dimensionality and Chemical Families

Inorganic electrides are classified geometrically by the dimensionality of the interstitial space occupied by the anionic electrons (**Fig. 1**) and chemically by the bonding nature of the host lattice. In C12A7:e^-,



the anionic space is zero-dimensional (0D, **Fig. 1a**): the cubic mayenite framework contains 12 cages of ~0.4 nm internal diameter per unit cell, interconnected by ~0.1 nm openings, and electron transport proceeds by variable-range hopping at low doping or band-like conduction at high cage occupancy [4-5]. Two of the twelve cages per unit cell are occupied by extra-framework O^{2-} ions in stoichiometric mayenite; replacing those oxygen anions with electrons yields carrier concentrations up to 2.1–2.3 × 10^{21} cm^{-3}, driving an insulator-to-metal transition near 1 × 10^{21} cm^{-3} and room-temperature electrical conductivities up to ~1500 S cm^{-1} [4, 7].

Fig. 1 Structural classification of inorganic electrides by anionic electron dimensionality. **(a)** Zero-dimensional (0D) cage electride exemplified by $[Ca_{24}Al_{28}O_{64}]^{4+}(e^-)_4$ (C12A7:e^-), in which electrons occupy subnanometer (~0.4 nm) cages of the mayenite lattice and hop or tunnel through ~0.1 nm cage windows [4, 7]. **(b)** One-dimensional (1D) channel electride exemplified by hexagonal Sr_5P_3 (Mn_5Si_3-type structure), in which anionic electrons are confined along linear chains parallel to the *c*-axis [16]. **(c)** Two-dimensional (2D) layered electride exemplified by $[Ca_2N]^+\cdot e^-$ or $[Y_2C]^{2+}\cdot 2e^-$, where anionic electrons form a delocalised 2D electron gas within the interlayer gallery [17-18]. Dimensionality governs conduction anisotropy, facet-dependent work functions, and mechanical exfoliability.

One-dimensional (1D) electrides confine anionic electrons along crystallographic channels or chains within the cation sublattice. Strontium phosphide (Sr_5P_3) is a structurally characterised prototype (**Fig. 1b**): it crystalizes in a hexagonal Mn_5Si_3-type framework in which anionic electrons occupy 1D channels running parallel to the *c*-axis [16]. Notably, while density functional theory (DFT) within the generalized gradient approximation predicts metallic conduction along the chains, experimental transport and photoemission measurements on synthesized Sr_5P_3 reveal a Mott-insulating/semiconducting state with a narrow ~0.1 eV band gap arising from strong electron correlation in the half-filled 1D anionic band [16]. True metallic 1D channel conduction is realized in the isostructural silicide $[Y_5Si_3]^{0.8+}\cdot 0.8e^-$ [19], apatite-type channel oxides such as $La_8Sr_2(SiO_4)_6{:}4e^-$ [20], and the transition-metal chalcogenide $[Ti_2S]^{2+}\cdot 2e^-$ [21].

Two-dimensional (2D) electrides host anionic electrons within the van der Waals-like gallery between positively charged cationic slabs. Anti-$CdCl_2$-type $[Ca_2N]^+\cdot e^-$ is the foundational example (**Fig. 1c**): Lee et al. measured a low-temperature Hall mobility of 520 $cm^2\ V^{-1}\ s^{-1}$ and a carrier mean free path of 0.12 μm, demonstrating that the work function is strongly facet-dependent—2.6 eV on the cleavage plane exposing the interlayer electron gas versus 3.5 eV perpendicular to it [17]. $[Y_2C]^{2+}{:}2e^-$ and $[Gd_2C]^{2+}{:}2e^-$ are isostructural rare-earth carbide analogues with higher nominal electron densities and *d*-orbital hybridization [18, 22].

From a device-processing standpoint, a crucial development is the discovery of electride families that overcome the severe air and moisture sensitivity of early alkaline-earth nitrides and carbides through two distinct chemical mechanisms: (i) kinetic surface self-passivation and (ii) intrinsic intermetallic framework stabilization. In the self-passivating chalcogenides $[Hf_2S]^{2+}\cdot 2e^-$ and $[Ti_2S]^{2+}\cdot 2e^-$, the surface reacts rapidly with ambient oxygen to form a dense, self-limiting native oxide layer (~10 nm amorphous HfO_2 or TiO_2) that kinetically blocks further oxidation, enabling the bulk material to survive immersion in water and strong acids [21, 23]. However, an insulating native oxide shell is not the only route to stability in electronic devices, nor is it always the preferred one, because

a 10 nm dielectric skin can impede interfacial charge transfer at low bias. Equally important is the growing class of intermetallic electrides, including binary silicides such as Y_5Si_3 [19], ternary LaTMSi compounds (TM = Sc, Co, Fe, Mn) [24-26], and ternary A_2BC_2 carbides/silicides [12]. In these intermetallic electrides, strong covalent/metallic bonding within the transition-metal/main-group framework and multicentre orbital hybridisation with the interstitial electrons confer chemical durability of the bulk phase in ambient air and water without a thick insulating passivation shell, while maintaining low-to-moderate work functions (2.7 to 4.0 eV on air-exposed polycrystals) and metallic conductivity. These values already include the native surface layer and are the correct input for design. The relevant question is whether the barrier rise is recoverable and whether any shell stays thin enough to tunnel through.

A phase variant of major practical importance for thin-film optoelectronics is amorphous C12A7:e^- (*a*-C12A7:e^-). Rapidly quenched C12A7:e^- glass and room-temperature-sputtered amorphous films retain an anionic electron concentration comparable to the crystal (~0.8×10^{21} cm^{-3} by iodometry) while exhibiting a wide optical gap (~5.3 eV) and low bulk conductivity (~10^{-8} S cm^{-1} at room temperature) [27]. Insulating bulk transport would spoil a standalone electrode. Even so, a 3.0 eV work function, nanometer-scale tunnelling thickness, and room-temperature sputter deposition make this material ideal for an ultrathin electron-injection interlayer. This approach bypasses the ~950 °C crystallisation budget of crystalline C12A7:e^-, which precludes glass and flexible polymer substrates (Section 4.2).

2.2 Device-Relevant Figures of Merit and Work-Function Metrology

For electronic device design, the relevant material parameters reduce to three: the work function φ, the electrical conductivity (σ) or carrier mobility (μ) of the anionic electrons, and the chemical stability of the material under fabrication and operating environments. **Table 1** compiles these parameters across oxide, nitride, carbide, chalcogenide, and intermetallic electrides, and **Fig. 2** benchmarks their

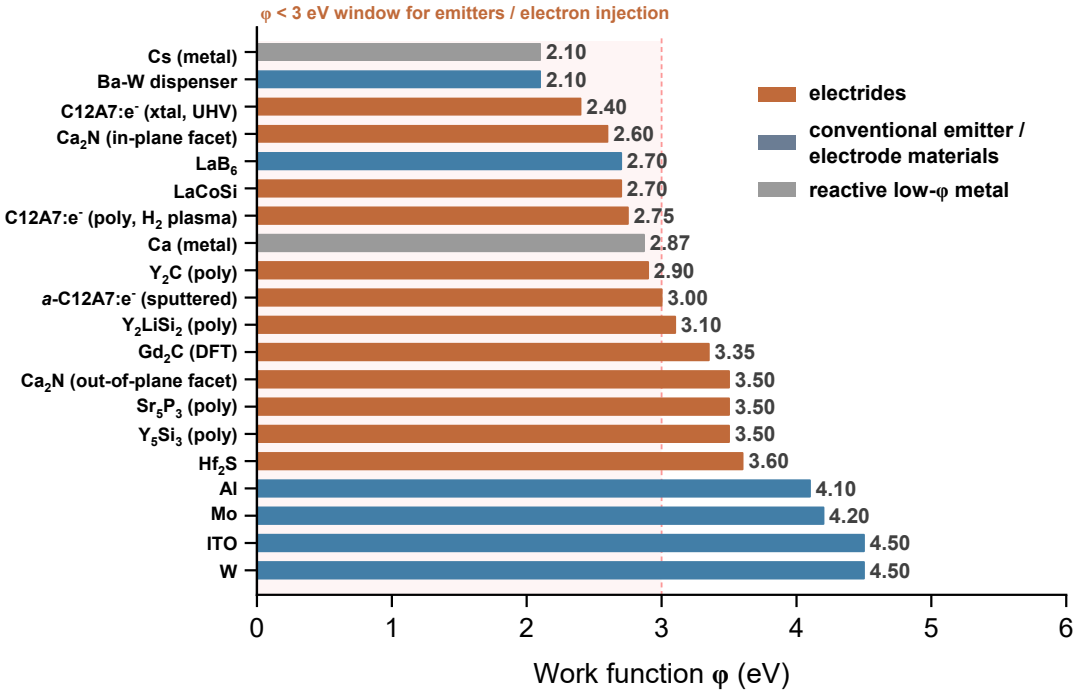
reported work functions against conventional emitter/electrode materials and reactive low-φ alkali/alkaline-earth metals.

Table 1 Device-relevant physical and chemical properties of representative inorganic electrides. E = experimentally measured; T = theoretically predicted (DFT) or nominal value from stoichiometry. Work-function entries are tagged as φ_{surf} (measured surface work function), φ_{DFT} (calculated intrinsic value) or φ_{app} (apparent barrier from emission or tunnelling analysis), with the measurement method and surface condition noted.

Material	**Electron space**	n_e **(cm^{-3})**	**Transport (RT)**	φ **(eV) — method**	**Ambient behaviour & stabilisation mechanism**	**Ref.**
$[Ca_{24}Al_{28}O_{64}]^{4+}(4e^-)$ single crystal	0D cages	≤2.1–2.3 × 10^{21} (E)	σ ≤ ~1500 S cm^{-1}; MIT near 1 × 10^{21} cm^{-3} (E)	2.4 (φ_{surf}; UPS/PYS, clean surface, UHV)	Handleable in air; reversible hydroxide/carbonate surface skin	[4, 7, 28]
C12A7:e$^-$, melt-solidified polycrystal	0D cages	~3 × 10^{19} (E)	σ ≈ 5 S cm^{-1} (E)	0.6 (φ_{app}; Fowler–Nordheim slope, not a work function)	As above	[29]
a-C12A7:e$^-$, RT-sputtered film	0D cage-like voids	~0.8 × 10^{21} (E, iodometry)	σ ≈ 10^{-8} S cm^{-1}; Tauc gap ~5.3 eV (E)	3.0 (φ_{surf}; UPS, as-deposited film)	Stable in device stacks; RT process	[27]
Sr_5P_3 polycrystal	1D channels	\	Mott semiconductor, E_g ≈ 0.1 eV (E); DFT-GGA predicts a metal (T)	3.5 (φ_{surf}; UPS, polycrystal)	Air-sensitive; handled in Ar	[16]
$[Y_5Si_3]^{0.8+}\cdot 0.8e^-$ (intermetallic)	1D channels	~0.8 e$^-$ per f.u. (T, nominal)	Metallic (E)	3.5 (φ_{surf}; PYS, polycrystal)	Intrinsically air- and water-durable (covalent/metallic framework)	[19]
LaTMSi (e.g., LaFeSi, LaCoSi; intermetallic)	0D tiered voids	\	Metallic (E)	2.7–3.2 (φ_{surf}; UPS, air-exposed polycrystal)	Intrinsically air- and water-durable (TM–Si framework hybridisation)	[24-26]
A_2BC_2 series (e.g., Y_2LiSi_2; intermetallic)	0D voids	Variable (T)	Metallic (E)	3.1-4.0 (φ_{surf}; UPS, E); 2.45–3.8 (φ_{DFT}; facet-dependent, T)	High intrinsic chemical stability in air and moisture	[12]
$[Ca_2N]^+\cdot e^-$	2D interlayer gas	~1.4 × 10^{22} (T, nominal)	μ = 520 cm^2 V^{-1} s^1; mean free path 0.12 μm (E, low T)	2.6 in-plane / 3.5 out-of-plane (φ_{surf}; UPS, cleaved facets)	Reacts rapidly with moisture and air; requires inert atmosphere	[17, 30]
$[Y_2C]^{1.8+}\cdot 1.8e^-$	2D interlayer gas	~2.9 × 10^{22} (T, nominal)	Semimetallic; paramagnetic, ~0.6 μ_B per Y (E)	2.9 (φ_{surf}; PES, polycrystal, E); 3.51 (φ_{app}; STS, cleaved surface, E)	Inert-atmosphere handling	[18]
$[Gd_2C]^{2+}\cdot 2e^-$	2D interlayer gas	~2.8 × 10^{22} (T, nominal)	Ferromagnetic metal, T_C ≈ 350 K, ~0.52 μ_B per e$^-$ (E)	3.35 (φ_{DFT}, T); no measured value reported	Inert-atmosphere handling	[22]

$[Hf_2S]^{2+}\cdot 2e^-$	2D interlayer gas	\	Metallic (E)	3.6 (φ_{surf}; UPS)	Kinetically self-passivating (~10 nm native HfO_2); water/acid-stable	[23]
$[Ti_2S]^{2+}\cdot 2e^-$	1D channels	\	Metallic (E)	~3.5 (φ_{surf}; UPS)	Kinetically self-passivating (native TiO_2); water/acid-durable	[21]

Among these parameters, the work function is the most frequently contested, with literature values for a single nominal compound spanning more than 4 eV. For C12A7:e^- alone, published reports include 0.6 eV (extracted from Fowler–Nordheim plots of planar field emission) [29], 2.4 eV



(ultraviolet and photoelectron yield spectroscopy on a clean single-crystal surface in ultrahigh vacuum) [28], 2.75 ± 0.10 eV (steady state under low-pressure hydrogen plasma exposure) [31], 3.0 eV (room-temperature-sputtered amorphous film) [27], and nearly 5.0 eV for an as-received, air-exposed polycrystalline surface [31].

Rather than representing experimental error, these numbers probe physically distinct surfaces. The intrinsic vacuum work function of clean crystalline C12A7:e^- sits near 2.4 eV [28]. Ambient exposure rapidly forms a hydroxide and carbonate surface skin that raises the effective surface barrier by more than 2 eV; vacuum annealing or hydrogen/helium plasma bombardment strips this skin, and Heiler et al. tracked the barrier relaxing back at roughly +0.6 eV h^{-1} once plasma exposure ceased [31].

Fig. 2 Benchmark of work functions for electrides, conventional emitter/electrode materials (slate blue), and reactive low-φ metals (grey). All values are experimentally measured. The shaded region marks the $\varphi < 3$ eV window for efficient thermionic/field emission and barrier-free electron injection into organic semiconductors. Air/water-stable intermetallic (LaCoSi, Y_2LiSi_2, Y_5Si_3) and self-passivating (Hf_2S) electrides fall at 2.7–4 eV, still ~1 eV below refractory metals (Mo, W). The 0.6 eV Fowler–Nordheim slope value for polycrystalline C12A7:e^- is excluded as it does not represent a true vacuum-level work function. Because values were obtained under different surface conditions and by different techniques, the figure should be read as a compilation rather than a like-for-like ranking. Data from refs. [12, 16-19, 22-23, 25, 27-28, 31].

Conversely, the widely cited 0.6 eV value is an *apparent* barrier derived from Fowler–Nordheim slope analysis, which conflates local geometric field enhancement and upward band bending across a semiconducting surface depletion layer. A comparable methodological divergence appears in Y_2C, where photoelectron spectroscopy on polycrystalline samples yields 2.9 eV whereas scanning tunnelling spectroscopy on a cleaved surface yields 3.51 eV [18]. Consequently, an electride work function quoted without its measurement technique, base pressure, and surface preparation history has limited value for quantitative device modelling.

2.3 Thin-Film Deposition, Bulk Synthesis, and Device Integration Routes

Synthetic routes to electrides have progressed substantially toward device-compatible forms. Early C12A7:e^- single crystals were prepared by annealing stoichiometric mayenite in sealed calcium or titanium vapour at ~1100 °C for several days—an approach suitable for intrinsic transport physics but incompatible with wafer-scale manufacturing [4, 7]. Kim et al. subsequently demonstrated direct synthesis of polycrystalline C12A7:e^- by solidifying a carbon-reduced melt and crystallising oxygen-deficient glasses, yielding machinable monoliths with $\sigma \approx 5$ S cm^{-1} suitable for emitter inserts [29]. Intermetallic electrides such as Y_5Si_3 and LaTMSi are readily synthesised in bulk ingots via standard arc-melting and solid-state annealing [19, 24], offering straightforward target fabrication for physical vapour deposition. For thin-film devices, pulsed-laser deposition followed by post-annealing produces crystalline epitaxial films [7], whereas radio-frequency magnetron sputtering from a conductive C12A7:e^- or composite target at room temperature yields smooth amorphous films ($R_a \approx 0.6$ nm) [27, 32]. Top-down dry etching combined with electron doping has also produced C12A7:e^- nanowires

with room-temperature conductivities of ~6 S cm^{-1} [33]. Druffel et al. studied 2D layered electrides. They demonstrated liquid-phase exfoliation of $[Ca_2N]^+ \cdot e^-$ into few-layer nanosheets. This result is consistent with the low computed cleavage energy of 1.11 J m^{-2}. The nanosheets remained structurally intact for at least one month in anhydrous nitrogen-purged solvents [30].

What remains absent from the processing toolkit is a conformal, low-temperature vapour-phase deposition route (such as atomic layer deposition or low-temperature chemical vapour deposition) capable of producing crystalline electrides within back-end-of-line (BEOL) thermal budgets (< 400 °C). Furthermore, systematic fab-compatibility data—wet and dry etch selectivities, photoresist and developer compatibility, and chemical-mechanical polishing (CMP) behaviour—have not been established for any electride family. As discussed in Section 7, these integration gaps impose stricter constraints on device adoption than intrinsic bulk electronic properties.

3. Vacuum Electron Sources and Plasma Emitter Devices

Electron emission represents the most mature hardware application of electrides (**Table 2**). **Table 3** provides quantitative comparisons with the incumbent technology for each device category. Because emission current density depends exponentially on the work function in both the thermionic (Richardson–Dushman) and cold-field (Fowler–Nordheim) regimes, lowering φ while retaining a refractory framework eliminates the poisoning vulnerability and heater overhead that plague caesiated surfaces and barium-dispenser cathodes.

Table 2 Summary of reported electride-based electronic devices and candidate electrode families alongside their key experimental or simulated figures of merit.

Device category	Active electride & phase	Device role / architecture	Fabrication & operating conditions	Key measured / predicted figures of merit	Reported endurance / stability	Evidence level & Ref.
Cold field emitter	Melt-solidified polycrystalline C12A7:e^-	Planar cold cathode (polished flat surface)	Melt-solidification at 1600 °C; RT vacuum emission	J = 12 μA cm^{-2} at E = 2.4 × 10^5 V cm^{-1}; apparent FN barrier 0.6 eV	Stable short-term UHV operation	Device hardware [29, 34]
Thermal-field emitter	Single-crystal C12A7:e^- tip (80 μm spot)	Thermal-field emission gun cathode	≤ 900 °C at 10^{-5} Pa (well below LaB_6)	I ≈ 50 μA emission current; non-	> 90 h continuous operation	Device hardware [35]

				alloying with support		
Hollow cathode (electric propulsion)	Polycrystalline C12A7:e^- cylindrical insert	Heaterless hollow cathode / plasma neutraliser	Xe or I_2 propellant; room-temperature heaterless ignition	2 A continuous discharge; back-contact metallurgy (TiCuNi vs. Ag) governs I–V	> 50 h (Rand) to > 950 h (Drobny); thermal melting limit	Device hardware [36-38]
Cs-free H^- ion source grid	Plasma-pretreated polycrystalline C12A7:e^-	Surface-conversion plasma grid on kW-class EVISS source	In situ H_2 plasma activation (φ stabilises at 2.75 ± 0.10 eV)	+70 % extracted H^- beam current vs. Al reference grid without Cs	~10 h steady φ under plasma; relaxes at +0.6 eV h^{-1} off-plasma	Device hardware [31, 39]
Thermionic energy converter (PETE)	Polycrystalline C12A7:e^-	Photon-enhanced thermionic cathode	500 °C under optical illumination	J = 5 mA cm^{-2} thermionic current; only ~1 % photo-enhancement (surface dielectric barrier)	Not life-tested	Device hardware (negative result) [40]
Inverted OLED	Amorphous a-C12A7:e^- (4 nm) / a-ZSO (40 nm)	Electron-injection & hole-blocking bilayer cathode	Room-temperature RF sputtering (R_a ≈ 0.6 nm); compatible with oxide TFTs	$V_{turn\text{-}on}$ lowered from 9.2 V (LiF/Al) to 4.7 V; IE = 7.9 eV blocks holes	Initial J–V–L reported; long-term operational lifetime unverified	Device hardware [27, 32, 41]
Resistive switching memory	Surface-oxidised single-crystal & ceramic C12A7:e^-	Pt / C12A7:O^{2-} / C12A7:e^- / Pt memristive cell	Field-driven cage O^{2-}/e^- redox exchange at ±5 V	On/off ratio ~10^2; non-filamentary bulk/interfacial cage switching	180–1000 cycles after electroforming	Device hardware [42-44]
2D semiconductor FET contacts	2D $[Ca_2N]^+ \cdot e^-$ or Ca_2XY_2 (brominated)	Donor–acceptor van der Waals / quasi-bonded source–drain contacts to MoS_2, ZrS_2, MSi_2N_4	First-principles DFT + NEGF quantum transport simulation	100 % tunnelling probability; intrinsic Ohmic contact; I_{on} ≈ 10^4 μA μm^{-1} at 0.2 V bias	No experimental transistor fabricated (air/lithography sensitivity)	Theory / simulation only [45-48]
Spintronic tunnel junctions	2D ferromagnetic $[Gd_2C]^{2+} \cdot 2e^-$ or $FeCl_2/Ca_2N$	Spin-polarised interstitial electron injector	Bulk crystal synthesis (T_C ≈ 350 K) & heterostructure DFT	0.52 μ_B per anionic electron in interlayer voids; room-temperature ferromagnetism	No experimental MTJ or spin valve reported	Materials data & theory [14, 22]

Table 3. Quantitative comparison of electride devices with incumbent technologies.

Application	**Incumbent benchmark and operating conditions**	**Quantified advantage / remaining gap**

Cold field emitter	Vertically aligned CNT arrays: turn-on ~3.25 V μm^{-1}, ~30 mA cm^{-2} at ~4 V μm^{-1} [49]	Electride delivers ~2500× lower current density at ~6× higher macroscopic field. Advantage is planar geometry and absence of tip erosion, not emission efficiency. No endurance data
Thermal-field gun	LaB_6: ~1500–1600 °C, high-purity vacuum [7, 35]	At least 600 °C lower operating temperature, tolerance of 10^{-5} Pa and no chemical interdiffusion with refractory-metal supports demonstrated; reduced brightness and energy spread not reported
Hollow cathode	BaO–W ~1300 °C, LaB_6 ~1500–1600 °C [50-51]; LaB_6 ignition ~200 W heater vs. ~30 W for C12A7:e^- in the same testbed [52]; BaO–W life test 28,000 h [53]	Heaterless room-temperature ignition; ~1000–1100 °C insert [51]; iodine compatibility unique [36]. ~30× lifetime gap (>950 h vs. 28,000 h); ceiling set by melting (~1400 °C) and decomposition (>1100 °C) [51-52]
H^- converter grid	Cs/Mo plasma grid, $\varphi \approx 2.1$ eV. ITER NBI requirement: 329 A m^{-2} (H^-), 286 A m^{-2} (D^-) at 0.3 Pa, the target of the caesiated ELISE RF source [54]	+70% extracted H^- vs. Al reference without caesium [39]; $\varphi_{op} = 2.75 \pm 0.10$ eV for ~10 h [31]. Absolute current density far below ITER-class values; suited to small and medium sources
PETE converter	Not benchmarked; no competitive electride result reported	5 mA cm^{-2} at 500 °C but only ~1% photo-enhancement [40]; the surface skin quenches the photo-response (Section 3.3)
Inverted OLED	LiF/Al inverted 9.2 V, bare Al 11.1 V, conventional LiF/Al 5.7 V [27]; solution-processed nc-ZnO EIL: 25.5 cd A^{-1}, LT50 > 2000 h at 100 cd m^{-2} [55]	Turn-on reduced by 4.5 V (−49%) vs. inverted LiF/Al at equal or higher current efficiency; RT sputtering and hole blocking (IE = 7.9 eV). Operational lifetime unreported
Resistive memory	HfO_x/TaO_x RRAM: endurance >10^8 cycles, with faster switching and a larger memory window [56]	On/off ~10^2, ±5 V, 180–1000 cycles [42-44]: five to six orders of magnitude short in endurance. Value is as a model nanoionic system, not a commercial memory
2D-material contact	Bi/monolayer MoS_2: R_c = 123 Ω μm, I_{on} = 1135 μA μm^{-1} at 1 V [57]; Sb(01-12)/MoS_2: R_c = 42 Ω μm, I_{on} = 1.23 mA μm^{-1}, stable at 125 °C [58]	Predicted 100% tunnelling probability and $I_{on} \approx 10^4$ μA μm^{-1} at 0.2 V [46-48] are ballistic ideal-interface upper bounds; no measured R_c exists. Target: $R_c \lesssim 100$ Ω μm after ambient processing
Magnetic tunnel junction	CoFeB/MgO/CoFeB: TMR 604% at 300 K [59]	$T_C \approx 350$ K and 0.52 μ_B per anionic electron measured in Gd_2C [22]; no TMR, no spin-injection measurement, no MTJ reported

3.1 Cold Field Emission and Thermal-Field Emission Cathodes

Dye and co-workers demonstrated thermionic electron emission from organic electride and alkalide films at cryogenic temperatures (−80 °C) as early as 1990 and quantified its barrier energetics in 2000 [60-61], but rapid thermal degradation prevented room-temperature operation. Following the discovery of C12A7:e^-, Toda et al. demonstrated cold field emission from its encaged electrons in 2004 [34], and in 2006 Kim et al. reported a benchmark planar emission current density of 12 μA cm^{-2} at an applied electric field of 2.4 × 10^5 V cm^{-1} from a flat, mirror-polished polycrystalline disk [29]. The technological significance lies in the planar geometry: conventional cold field emitters rely on sharp Spindt tips or high-aspect-ratio nanotubes to achieve local field enhancement, which introduces tip-to-tip current non-uniformity and sputter erosion, whereas a flat low-φ oxide emitter simplifies array lithography and electrostatic optics.

Thermal-field emission bridges the gap to higher continuous currents. Toda et al. extracted ~50 μA from an 80 μm emitting spot on a C12A7:e^- single-crystal needle at temperatures ≤ 900 °C under a moderate vacuum of 10^{-5} Pa, maintaining stable emission for more than 90 h without degradation [35]. Relative to commercial LaB_6 cathodes (~1500–1600 °C), C12A7:e^- operates at substantially lower temperature, tolerates poorer vacuum, and does not chemically interdiffuse with refractory metal supports.

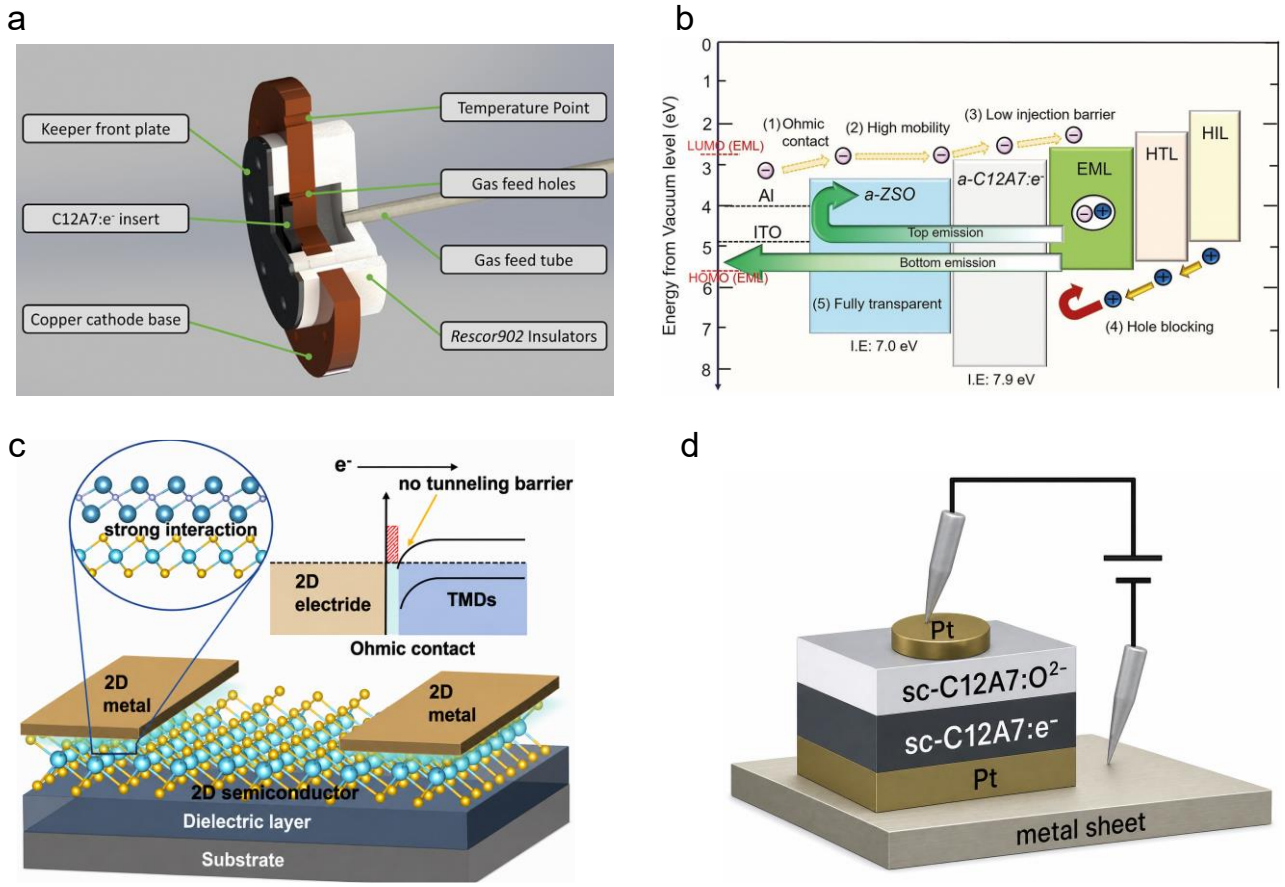
3.2 Heaterless Hollow Cathodes for Space Electric Propulsion

Space electric propulsion is the domain where electride devices have progressed furthest toward field deployment. Hollow cathodes supply electrons to ionise propellant gas and neutralise the exhaust plume of gridded ion and Hall-effect thrusters, and cathode wear or heater failure routinely limits mission lifetime. Current barium-oxide-impregnated tungsten (BaO–W) inserts are rapidly poisoned by trace oxygen or water, which necessitates the use of costly ultra-high-purity xenon. In comparison, LaB_6 inserts require operation at approximately 1600 ℃ and the use of reactive-metal barriers. Both

architectures typically rely on an external resistive heater for ignition, which represents a primary single-point failure mode.

C12A7:e^- addresses these vulnerabilities simultaneously by resisting oxygen poisoning as an oxide and emitting at temperatures several hundred degrees below those of LaB6. Furthermore, according to the experimental assessment of Kottke et al. [36], it is the only low-work-function emitter material demonstrating chemical compatibility with iodine vapour, a high-density storable propellant increasingly favoured for small-satellite constellations. Rand and Williams constructed a 6 mm C12A7:e^- hollow cathode that operated on xenon for > 50 h without measurable erosion and ignited directly from room temperature without an external heater [37]. The TU Dresden group subsequently extended endurance testing to propulsion-qualification timescales: a heaterless plasma cathode incorporating a C12A7:e^- insert (**Fig. 3a**) achieved more than 950 h of continuous operation at 2 A discharge current, the longest endurance reported for an electride device [38]. Post-test microstructural analysis revealed localised melting of the insert rather than bulk electron depletion, demonstrating that the operational ceiling is governed by low thermal conductivity and local plasma heating rather than work-function degradation.

Systematic fabrication studies by Kottke et al. revealed counter-intuitive engineering constraints that govern cathode yield [36]. Whereas mechanical grinding and polishing are routine preparation steps for metallic emitters, abrasive machining of C12A7:e^- degrades electron emission by damaging the surface cage network. Cation substitution with barium or strontium expands the lattice cages and enhances emission current. Most critically, the back-side electrical contact dominates overall device impedance: silver paste and reactive TiCuNi brazing produce markedly different current–voltage characteristics, and a high-resistance back contact masks the intrinsic emission capability of the front surface [36]. Furthermore, C12A7:e^- cathodes exhibit pronounced transient conditioning behaviour over tens of hours that is absent in LaB_6 references, underscoring that short laboratory test runs cannot predict steady-state thruster performance.



3.3 Caesium-Free Converter Electrodes for Negative Hydrogen Ion Sources

Neutral beam injection (NBI) heating systems for magnetic-confinement fusion reactors and high-intensity particle accelerators require multi-ampere negative hydrogen or deuterium ion (H^-/D^-) beams. Current sources generate H^- via surface conversion of plasma atoms and positive ions on a molybdenum plasma grid coated with evaporated caesium ($\varphi \approx 2.1$ eV). Although effective, continuous caesium injection causes electrode sparking, high-voltage insulator contamination, and complex maintenance schedules. A solid, caesium-free low-φ converter grid would eliminate an entire hazardous subsystem.

Fig. 3 Representative electronic device architectures incorporating inorganic electrides. **(a)** Heaterless hollow cathode with a cylindrical C12A7:e^- emitter insert for space electric propulsion, capable of room-temperature ignition and > 950 h continuous operation [38]. **(b)** Energy-level diagram and stack architecture of an inverted OLED employing a 4 nm room-temperature-sputtered amorphous *a*-C12A7:e^- electron-injection layer paired with an amorphous ZnO–SiO_2 (*a*-ZSO) electron-transport layer [27]. **(c)** Schematic of a two-dimensional electride/transition-metal dichalcogenide (Ca_2N/TMD) heterostructure contact, in which the interlayer anionic electron gas suppresses both the van der Waals tunnelling barrier and Fermi-level pinning [46-47]. **(d)** Non-filamentary resistive switching memory cell based on field-driven O^{2-}/e^- redox exchange across a surface-oxidised C12A7:e^- crystal [42]. Panels (a), (b), (c), and (d) are reprinted with permission from

refs [38], [27], [47], and [42], respectively. © 2023 Elsevier Ltd., © 2017 National Academy of Sciences, © 2008 American Chemical Society, and © 2008 Elsevier B.V.

Heiler et al. evaluated polycrystalline C12A7:e^- converter surfaces *in situ* under low-pressure, low-temperature hydrogen plasma exposure [31]. Starting from an air-exposed barrier near 5.0 eV, plasma bombardment reduced and stabilised the surface work function at 2.75 ± 0.10 eV for ~10 h of continuous operation, relaxing at ~0.6 eV h^{-1} after plasma shutdown. Vacuum thermal annealing alone recovered a degraded surface only to 2.9 eV at 670–770 K. Notably, the authors observed that H^- yield did not scale with work function according to standard metallic resonant-tunnelling models, indicating that surface H^- conversion on a nanoporous oxide electride involves distinct electronic states [31]. At the full beamline level, Nakano et al. installed a plasma-pretreated C12A7:e^- grid on the kilowatt-class Equipment with Versatility for Ion Source Study (EVISS) negative ion source and demonstrated a 70 % increase in extracted H^- beam current compared with an aluminium reference grid [39]. Because the plasma grid is a single replaceable electrode component, caesium-free ion sources represent one of the highest-leverage near-term applications for bulk electrides.

3.4 Photon-Enhanced Thermionic Energy Conversion and Surface Limitations

Not every electron-emission architecture has succeeded, and negative results clarify the underlying material limits. Toledo et al. evaluated C12A7:e^- as the cathode of a photon-enhanced thermionic emission (PETE) solar converter, measuring 5 mA cm^{-2} of baseline thermionic current at 500 °C but only ~1 % current enhancement under optical illumination [40]. Efficient PETE operation requires photoexcited electrons from the bulk cage conduction band to reach the vacuum interface without recombination; the self-formed dielectric hydroxide/carbonate surface layer on air-handled C12A7:e^- acts as a transport bottleneck—the exact same surface skin responsible for the work-function spread analysed in Section 2.2.

4. Charge-Injection Interlayers in Organic and Thin-Film Optoelectronics

4.1 Energy-Level Alignment and Electron-Injection Barriers at Organic Interfaces

Efficient electron injection into organic semiconductors requires minimising the energy offset between the cathode Fermi level and the lowest unoccupied molecular orbital (LUMO) of the organic transport layer. The usual commercial cathode is a very thin LiF layer beneath aluminium. At the Alq3 interface, it still leaves an electron-injection barrier of about 1.4 eV. Alq3 stands for tris(8-hydroxyquinolinato)aluminium. The cathode works through interfacial dipole formation and partial Li liberation. Using *in situ* ultraviolet photoelectron spectroscopy (UPS), Kim et al. measured an electron-injection barrier of only 0.6 eV at the crystalline C12A7:e^-/Alq_3 interface—less than half that of LiF/Al—accompanied by a 1.2 eV downward vacuum-level shift upon contact [62]. Yanagi et al. extended these interfacial measurements to pentacene, fullerene (C_{60}), and copper phthalocyanine (CuPc), confirming that low injection barriers are a general consequence of the electride's low work function rather than a specific chemical reaction with Alq_3 [63], and demonstrated early inverted OLED prototypes combining crystalline C12A7:e^- cathodes with $Cu_{2-x}Se$ hole-injection layers [41].

But there is a catch. Getting these low barriers on crystalline C12A7:e^- films took aggressive in situ surface preparation. That meant high-temperature vacuum annealing, then helium plasma bombardment. Even then, the treated surface showed $\varphi \approx 3.1$ eV. The intrinsic value is 2.4 eV [62-63]. Furthermore, amorphous C12A7:e^- offers a second, frequently overlooked electronic advantage: its exceptionally large ionisation energy (~7.9 eV) creates a deep valence-band offset that blocks holes while injecting electrons [27], a dual functionality unattainable with elemental low-φ metals.

4.2 Room-Temperature Sputtered Amorphous C12A7:e^- in Inverted OLEDs

Because crystallising C12A7:e^- requires ~950 °C annealing, crystalline films cannot be integrated onto commercial display glass or flexible polymer backplanes. The enabling breakthrough was the discovery by Hosono et al. that room-temperature RF magnetron sputtering from a C12A7:e^- glass target preserves a high concentration of anionic electrons (~0.8×10^{21} cm^{-3}) in an ultrasmooth amorphous film (R_a = 0.6 nm, φ = 3.0 eV, optical gap ~5.3 eV) [27, 32]. By pairing a 4 nm *a*-C12A7:e^- electron-injection layer with a 40 nm amorphous $0.8ZnO{\cdot}0.2SiO_2$ (*a*-ZSO) electron-transport layer (φ

= 3.5 eV, $\mu_e \approx 1$ cm^2 V^{-1} s^{-1}, six orders of magnitude higher than Alq_3), Hosono et al. realised the first all-amorphous-oxide electron-injection stack for an inverted OLED (**Fig. 3b**) [27].

The resulting device metrics validate the amorphous-electride approach: the inverted OLED turned on at 4.7 V, outperforming not only inverted reference devices using LiF/Al (9.2 V) or bare Al (11.1 V) but also a conventional bottom-anode LiF/Al OLED (5.7 V) at equal or superior current efficiency [27]. Inverted OLED architectures are technologically critical for large-area active-matrix displays because high-mobility oxide thin-film transistor (IGZO TFT) backplanes are exclusively *n*-channel; connecting the OLED cathode directly to the bottom TFT drain eliminates current-crowding source-follower circuits and simplifies pixel compensation. In addition, the work function of *a*-C12A7:e^- can be continuously tuned between 3.0 and 3.5 eV by controlling the anionic electron concentration during sputtering, providing a practical knob for band-alignment engineering across diverse emitter chemistries [27].

4.3 Prospects in Perovskite and Quantum-Dot Optoelectronic Devices

Despite the success of *a*-C12A7:e^- in inverted OLEDs [27], we found no experimental reports applying electride interlayers to metal-halide perovskite light-emitting diodes (PeLEDs), colloidal quantum-dot LEDs (QLEDs) , or perovskite solar cells, even though interfacial electron extraction and non-radiative contact recombination limit all three technologies [64-66]. The primary concern is interfacial redox reactivity—placing a strongly reducing electride [17] directly against soft lead-halide octahedra risks reducing Pb^{2+} to metallic Pb^0 [67]. Whether a nanometer-thin *a*-C12A7:e^-/oxide bilayer or a chemically stable intermetallic electride film is kinetically compatible with halide perovskites under operational bias remains an untested, high-value experimental question.

5. Interconnects, Ohmic Contacts, and Channels in 2D Electronics

5.1 Two-Dimensional Layered Electrides as High-Mobility Conductors

The 2013 discovery of layered $[Ca_2N]^+ \cdot e^-$ sparked immediate anticipation that 2D electrides ("electrenes") would enter nanoelectronics as ultrathin metallic interconnects and low-barrier

electrodes [17]. Ca_2N has notable intrinsic transport. Its Hall mobility is 520 cm2 V^{-1} s^{-1}. The elastic mean free path is 0.12 μm. Its anisotropic magnetoresistance is pronounced. That confirms a true 2D electron gas inside a bulk crystal. Ca_2N also exfoliates in liquid phase into few-layer flakes [30]. Together, these properties put Ca_2N alongside graphene and metallic transition-metal dichalcogenides (TMDs).

That expectation has not yet translated into experimental nanoelectronic devices, and the barrier is chemical stability. $[Ca_2N]^+ \cdot e^-$ reacts quickly with moisture and oxygen in air. Exfoliated flakes can survive for weeks inside an inert nitrogen glovebox. They also survive in anhydrous organic solvents [30]. But standard semiconductor lithography destroys the anionic electron layer right away. That process includes spin-coating resist, aqueous alkaline development, oxygen plasma descum, and solvent lift-off. Unlike air-sensitive 2D semiconductors such as black phosphorus, where surface oxidation leaves a thinned semiconducting core, oxidation of a few-layer electride consumes the very interstitial electrons responsible for conduction. Overcoming this integration barrier does not depend on a single material mechanism, however: device engineers can draw on either intrinsically air- and water-stable intermetallic electrides (such as Y_5Si_3, LaTMSi, and A_2BC_2 compounds, which avoid forming thick insulating oxide barriers [12, 19, 24]), kinetically self-passivating layered chalcogenides such as $[Hf_2S]^{2+} \cdot 2e^-$ [23], or *in situ* surface functionalisation (e.g., bromination [46, 48]) and van der Waals encapsulation.

5.2 Van der Waals Ohmic Contacts to Two-Dimensional Semiconductors

High contact resistance (R_c) remains the primary performance bottleneck in scaled 2D TMD field-effect transistors (FETs). Direct physical vapour deposition of elemental metals damages the underlying monolayer lattice and pins the Fermi level near mid-gap via metal-induced gap states (MIGS), whereas gentle van der Waals transfer of pre-patterned metal electrodes avoids lattice damage at the cost of introducing a physical van der Waals tunnelling barrier. Two-dimensional electrides offer an elegant theoretical resolution: because their anionic electron gas extends outward into the interlayer

gallery beyond the cationic cores, placing a 2D electride against a 2D semiconductor populates the interfacial gap with delocalised charge, simultaneously suppressing the tunnelling barrier and mitigating Schottky barrier formation (**Fig. 3c**).

First-principles quantum transport calculations consistently support this mechanism across multiple independent groups. Wang et al. first modelled the 2D Ca_2N/MoS_2 donor–acceptor heterostructure and demonstrated intrinsic *n*-type Ohmic contact behaviour driven by interfacial charge transfer [45]. Tang et al. subsequently simulated contacts between Ca_2N and group-IV dichalcogenides MX_2 (M = Hf, Zr; X = S, Se), finding 100 % interfacial tunnelling probability, weak Fermi-level pinning, and an on-state current approaching 10^4 μA $μm^{-1}$ at 0.2 V drain bias for ZrS_2/Ca_2N FETs; crucially, they also showed that brominating the outer non-contact surface of Ca_2N greatly enhances ambient stability without degrading interfacial Ohmic injection [46]. Niu et al. generalised this 2D electron-gas contact paradigm across a broader family of 2D metal–semiconductor junctions [47], and Pan et al. recently demonstrated that 2D electride contacts (including Ca_2XY_2, X = Ti, Zr, Hf; Y = N, P) to MoS_2, WS_2, WSe_2, and MSi_2N_4 monolayers achieve 100 % tunnelling efficiency even when strong dipole-induced Fermi-level pinning coexists with Ohmic conduction [48].

In stark contrast to this burgeoning theoretical literature, not a single experimental transistor contacted with an electride has been reported to date (**Table 2**). Closing the theory–experiment gap is the key. It would define the single most decisive experiment in 2D electride electronics. Dry-transfer freshly cleaved Ca_2N inside an argon glovebox. Or deposit or transfer an intrinsically air-stable intermetallic electride, or a self-passivated chalcogenide electride. Put it onto a MoS_2 or ZrS_2 channel. Encapsulate the stack in hexagonal boron nitride (*h*-BN). Then extract the transfer-length contact Rc. Compare it with evaporated In/Au or Bi control electrodes on the same flake.

It is also worth clarifying a frequent terminological confusion in literature searches: published reports of "C12A7 FETs" utilise insulating, stoichiometric amorphous C12A7:O^{2-} as a high-*k* gate

dielectric ($\varepsilon_r \approx 12$) on oxide channels rather than using an electride as the conductive channel or contact [68].

5.3 Topological Electrides and Floating Surface States

Electrides provide a fertile structural platform for topological band structures because their interstitial anionic bands lie close to the Fermi level and experience weak nuclear attraction, promoting the band inversions required for non-trivial topology [11, 69]. In a foundational survey, Hirayama et al. identified Y_2C and Sr_2Bi as topological nodal-line semimetals, Sc_2C as a π-Zak topological insulator, HfBr as a quantum spin Hall insulator, and LaBr as a quantum anomalous Hall candidate [69].

From a device perspective, the standout parameter is the floating 2D surface charge density predicted for Sc_2C: 1.05×10^{15} electrons cm^{-2}, roughly equivalent to one electron per transition-metal site in a TMD monolayer, making cleaved Sc_2C an extreme electrostatic or charge-transfer doping substrate independent of its topological transport [69]. High-throughput screening by Guo et al. has since catalogued dozens of 3D topological inorganic electrides [11], though experimental device demonstrations remain entirely unexplored.

6. Emerging Device Concepts: Memory, Spintronics, and Superconductivity

6.1 Cage-Redox Resistive Switching Memories

Resistive random-access memory (RRAM) in C12A7:e^- operates by an ion–electron exchange mechanism fundamentally distinct from the stochastic oxygen-vacancy filament formation of conventional binary oxide (HfO_x, TaO_x) memristors. Adachi et al. demonstrated bistable resistance switching with an on/off ratio near 10^2 in a surface-oxidised C12A7:e^- single crystal (**Fig. 3d**), driven by electric-field-induced migration and redox exchange between encaged O^{2-} ions and anionic electrons within the rigid mayenite framework [42]. Yushkov et al. subsequently reproduced bipolar resistive switching at ±5 V in polycrystalline C12A7:e^- ceramics, demonstrating stable high- and low-resistance states over 180 to 1000 switching cycles following electroforming [43-44].

Evaluated strictly as non-volatile memory hardware, C12A7:e^- cells do not compete with commercial HfO_x arrays in switching speed, memory window, or endurance (> 10^8 cycles). Evaluated as a model nanoionic system, however, cage-confined O^{2-}/e^- exchange offers a structurally well-defined platform for studying bulk redox neuromorphic dynamics without destructive filament rupture [56, 70].

6.2 Ferromagnetic Electrides for Spintronics

Magnetic electrides open a compelling conceptual route toward solid-state spintronics [14, 22]. Lee et al. demonstrated that layered $[Gd_2C]^{2+}\cdot 2e^-$ is an intrinsic room-temperature ferromagnet with a Curie temperature (T_C) near 350 K and a magnetic moment of ~0.52 μ_B per anionic electron, originating from spin-polarised quasi-atomic interstitial electrons coupled to the Gd 4*f* local moments [22].

Because these spin-polarised carriers reside in the interlayer gallery outside the cationic cores, a ferromagnetic electride functions as a natural spin-injection source: the polarised electron gas is already positioned at the van der Waals interface where a tunnel barrier or 2D semiconductor channel meets the electrode [14-15]. Theoretical proposals have already explored magnetic heterojunctions such as $FeCl_2/Ca_2N$ [14], and extending spin-polarised transport studies to more chemically durable intermetallic magnetic electrides could accelerate the realisation of experimental magnetic tunnel junctions (MTJs) and spin valves.

6.3 Low-Temperature and High-Pressure Superconductivity

Bulk superconductivity in C12A7:e^- at T_c = 0.2–0.4 K (rising to 1.79–2.4 K under gigapascal hydrostatic pressure) established that cage-confined s-like anionic electrons can form Cooper pairs [71-72]. While high-pressure alkali-metal electrides such as Li_6P and Li_8Au reach much higher transition temperatures in diamond anvil cells [14], ambient-pressure electride superconductivity remains restricted to millikelvin regimes with no near-term electronic device utility.

7. Critical Bottlenecks in Device Integration and Reliability

Synthesizing the experimental record across Sections 3–6 reveals that the primary obstacles holding back electride electronics are not intrinsic bulk properties, but six interrelated integration bottlenecks, labelled B1 to B6 below.

7.1 (B1) Surface Chemical Evolution and Dual Pathways to Ambient Stability

The surface is chemically distinct from the bulk. Every device application reviewed above is governed by the top few nanometers of the electride: the 0.6 eV to 5.0 eV work-function spread in C12A7:e^- [28-29, 31], the suppression of photon enhancement in PETE converters [40], the mandatory plasma conditioning of H^- ion-source grids [31, 39], and the *in situ* vacuum/helium-plasma treatments required prior to organic semiconductor deposition [62-63]. For device engineers, the operative parameter is never the theoretical clean-facet work function, but the composition of the native surface after air transfer or solvent exposure. Critically, this surface change need not be permanent: the 2.6 eV barrier swing of C12A7:e^- is fully reversible under hydrogen plasma [28, 31], which is why it remains the only electride in working hardware despite having the largest documented work-function shift.

Ambient stability is achieved via two distinct mechanisms: intrinsic intermetallic bonding versus surface self-passivation. Across the electride family, ambient durability spans orders of magnitude, and it is crucial to recognize that high stability for electronic devices does not require relying exclusively on surface self-passivation.

In self-passivating chalcogenides ($[Hf_2S]^{2+}\cdot 2e^-$ and $[Ti_2S]^{2+}\cdot 2e^-$), the low-φ anionic electrons drive the rapid growth of a dense, self-limiting ~10 nm amorphous oxide layer (HfO_2 or TiO_2) that kinetically protects the underlying crystal against water and strong acids [21, 23]. While highly effective for electrocatalysis, a 10 nm insulating oxide skin can act as a series tunnelling barrier in vertical electronic contacts or low-bias emitters.

Fortunately, a second class of materials is growing rapidly. These are intermetallic electrides, which include binary silicides such as Y_5Si_3 [19][16], ternary LaTMSi compounds such as LaScSi, LaCoSi,

and LaFeSi [24], and ternary A_2BC_2 phases [12]. They exhibit remarkable intrinsic chemical stability in air and moisture without forming a thick insulating oxide shell. Their durability originates from stronger covalent/metallic bonding within the host lattice and partial multicentre hybridisation between framework *d*/*p* orbitals and interstitial electrons. Their durability originates from stronger covalent/metallic bonding within the host lattice and partial multicentre hybridisation between framework d/p orbitals and interstitial electrons. For device design, this distinction matters: a moderate barrier rise of a few tenths of an eV can be compensated by temperature or bias, whereas a thick insulating shell cannot. The native shell on $LaCu_{0.67}Si_{1.33}$ is about 3 nm [24], compared with the 10 nm oxide on self-passivating chalcogenides, making the intermetallic route more compatible with low-bias contacts.

Ranked alongside other families, C12A7:e^- (crystalline and amorphous) is structurally stable in ambient air despite reversible surface hydroxylation [6, 27], whereas rare-earth carbides (Y_2C, Gd_2C) require inert-gas handling [18, 22] and $[Ca_2N]^+ \cdot e^-$ decomposes rapidly in trace moisture [17, 30]. One caveat is that intrinsic stability has temperature limits: undoped Y_5Si_3 oxidises above about 700 °C to form a Y_2O_3 scale [73], which is below the 900 to 1100 °C thermionic window. Matching the stabilization mechanism and its operating envelope to the electrical requirements of the target device is therefore paramount.

7.2 (B2) Contact Metallurgy and Back-Contact Resistance

Kottke et al. provide a crucial lesson for the field. They show that back-contact brazing metallurgy, whether TiCuNi or Ag paste, dominates hollow-cathode emission characteristics. They also find that mechanical polishing of the emitting face degrades performance [36]. To date, standardized low-resistance Ohmic contact metallurgies have not been established for any bulk or thin-film electride.

7.3 (B3) Thermal Budget and Conformal Film Growth

The contrast between the ~950 °C crystallisation temperature of C12A7:e^- and the room-temperature sputtering of *a*-C12A7:e^- illustrates how decisively thermal budget dictates device compatibility [27].

Extending low-temperature sputtering or vapour-phase deposition to layered and intermetallic electrides is essential for their integration into standard CMOS or large-area display back-end flows.

7.4 (B4) Lithographic, Solvent and Patterning Compatibility.

No electride family has published fab-compatibility data. Wet- and dry-etch selectivities, photoresist and developer compatibility, and chemical-mechanical polishing behaviour are unknown. For 2D electrides the consequence is decisive, because the standard sequence of resist spin-coating, aqueous alkaline development, oxygen-plasma descum and solvent lift-off attacks the interlayer electron gas directly [30]. Unlike black phosphorus, where oxidation thins a semiconducting core, oxidation of a few-layer electride removes the carriers themselves. Three mitigation routes should be assessed comparatively: (i) inert-atmosphere dry transfer with *h*-BN encapsulation; (ii) in-situ surface functionalization, e.g. bromination of the non-contact face of Ca_2N [46, 48]; (iii) substitution with an intrinsically air-stable intermetallic electride, at the cost of a higher work function. Reporting the process flow alongside any device metric should become mandatory.

7.5 (B5) Work-Function Metrology and Reporting Standards

Cross-laboratory comparison of electride devices requires reporting four mandatory parameters alongside any work-function value: (i) the measurement technique (UPS, PYS, Kelvin probe, or thermionic/Fowler–Nordheim analysis), (ii) the base pressure during measurement, (iii) the exact surface cleaning or plasma activation protocol, and (iv) the cumulative exposure time to ambient or residual gas prior to acquisition. Furthermore, slope values extracted from Fowler–Nordheim field-emission plots on electrides should be strictly designated as apparent emission barriers rather than work functions, as standard Fowler–Nordheim theory assumes a free-electron metal with an abrupt vacuum boundary rather than a nanoporous oxide with surface band bending.

7.6 (B6) Operational Lifetime and Reliability Qualification

Outside the space-propulsion community, operational lifetime data for electride electronic devices are virtually non-existent (**Table 2**). By contrast, hollow cathodes in that field have been endurance-tested

for 50 to more than 950 h [37-38], and thermal-field emitters for more than 90 h [35]. Neither the *a*-C12A7:e^- inverted OLED [27] nor the C12A7:e^- memristive cells [42-44] have reported long-term operational stability (e.g., T_{80}: time to 80% of initial luminance under constant current stress or high-temperature data retention). Establishing device-level reliability metrics is essential before electrides can move from academic demonstrations to industrial qualification.

8. Conclusions and Future Outlook

Of the six bottlenecks identified in Section 7, four (B1 surface chemical evolution, B2 contact metallurgy, B3 thermal budget, B4 lithographic incompatibility) originate in the fundamental tension between a low vacuum work function and chemical reactivity. The remaining two (B5 work-function metrology, B6 operational lifetime) are infrastructural and can be resolved by community agreement and routine testing rather than by new materials chemistry. The highest-priority action is B5, since adopting the four-parameter reporting protocol costs nothing and immediately makes the existing literature comparable. The next priority is B1 + B2 + B6 for the hardware-validated C12A7:e^- family, where back-contact brazing, thermal management and published endurance data determine whether hollow cathodes and converter grids reach qualification. Third is B1 + B4 for the intermetallic and 2D track, whose decisive experiment is a glovebox-transferred, *h*-BN-encapsulated electride contact to a TMD channel with transfer-length-method R_c measured against evaporated In/Au or Bi controls on the same flake. The two agendas below address these priorities in parallel.

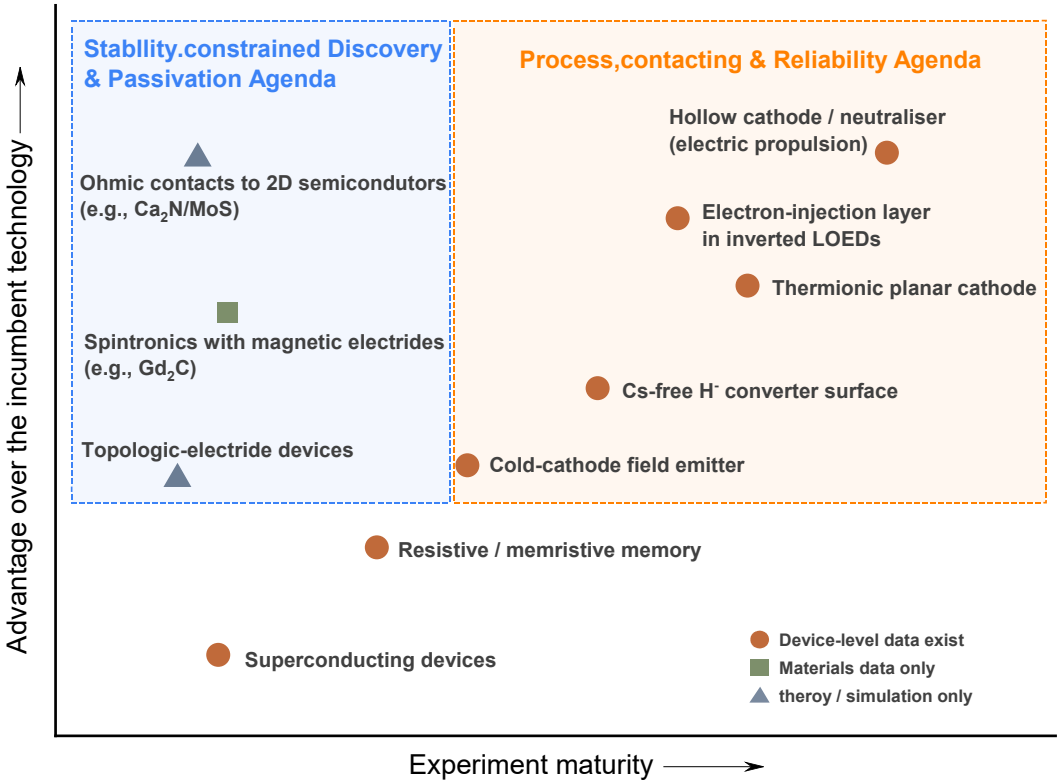
Crucially, the literature now demonstrates three viable strategies to resolve this tension for electronic devices: (i) amorphous phase engineering, exemplified by room-temperature-sputtered *a*-C12A7:e^-, which bypasses the 950 °C crystallisation step while preserving a 3.0 eV work function [27]; (ii) kinetic surface self-passivation, exemplified by Hf_2S and Ti_2S, where an ultrathin self-limiting native oxide protects the bulk against water and acid [21, 23]; and (iii) intrinsic intermetallic stabilisation, exemplified by Y_5Si_3 [19], LaTMSi [24], and A_2BC_2 [12] electrides, where framework

orbital hybridisation provides air and water durability without introducing a thick insulating oxide barrier.

Three tiers of material system can be distinguished by device evidence and remaining engineering risk. **Tier 1 (ready for engineering):** polycrystalline C12A7:e^- for heaterless hollow cathodes and caesium-free H^- converter grids, with endurance data at the hundreds-of-hours scale [37-38], and room-temperature-sputtered *a*-C12A7:e^- as a 4 nm electron-injection layer in inverted OLEDs [27]. The remaining tasks are contacting, thermal management and lifetime testing, not materials discovery. **Tier 2 (promising medium-term):** the intermetallic electrides Y_5Si_3, LaTMSi and the A_2BC_2 family, which combine metallic conduction, measured work functions of 2.7 to 4.0 eV, and bulk durability in air and water without a thick insulating oxide. Promotion to Tier 1 requires a working-device demonstration, together with processing and shape-forming routes that deliver the geometries electronics need (thin films, sputtering targets, needle or tip emitters, patterned contacts) rather than only bulk ingots from arc melting. **Tier 3 (exploratory):** Gd_2C for room-temperature spin injection ($T_C \approx 350$ K), and Ca_2N (brominated or *h*-BN-encapsulated) for Ohmic contacts to 2D semiconductors; both require fully inert-atmosphere processing. Four selection criteria apply to any new candidate for electronics: a measured $\varphi_{surf} \leq 3.5$ eV on an air-exposed surface, metallic room-temperature conduction, a native surface layer whose impact on barrier height and series resistance stays within the application tolerance, and a demonstrated processing route into the form factor required by the target device.

Future progress in electride electronics will therefore depend on two complementary agendas mapped in **Fig. 4**: engineering the compounds already validated in hardware (the right-hand zone) and translating chemically robust intermetallic and self-passivating electrides into device architectures where reactive compounds fail (the upper-left zone). Rather than competing for resources, each agenda supplies the constraints required by the other.

Agenda 1: Manufacturing, contacting, and qualifying existing hardware electrides. On the right-hand side of **Fig. 4**, working devices already exist. These include hollow cathodes, negative-ion



converter grids, and amorphous oxide OLED injection layers. In these cases, qualification cost dominates. Here, the priorities are concrete engineering tasks: (i) adopting the standardised work-function and surface-history reporting protocol outlined in Section 7.3; (ii) treating back-contact brazing, diffusion barriers, and thermal management in C12A7:e^- emitters as primary research subjects, including refractory-metal/electride composites and Ba/Sr lattice doping to prevent insert melting during > 1000 h thruster operation [36, 38]; (iii) developing low-temperature sputter or vapour-phase deposition routes for crystalline thin films; and (iv) publishing rigorous operational lifetime (T_{80}) and environmental stress data for *a*-C12A7:e^- optoelectronic interlayers.

Fig. 4 Technology maturity and R&D allocation map for electride electronic applications, plotting qualitative experimental maturity against projected performance advantage over incumbent technologies. Marker shapes denote the highest level of published evidence: circles represent working hardware devices with measured figures of merit, squares indicate materials-level characterisation without a fabricated electronic device (including ferromagnetic electrides and air-stable intermetallic electride electrodes), and triangles rest on first-principles calculations alone. The right-hand zone highlights hardware-validated domains where research should prioritise process engineering, contact metallurgy, and lifetime qualification; the upper-left zone highlights high-impact emerging concepts where progress depends on stability-constrained discovery (both intermetallic and self-passivating) and surface passivation.

Agenda 2: Exploiting intrinsically stable intermetallic electrides alongside self-passivating and encapsulated 2D electrides. In the upper-left quadrant of **Fig. 4**, reactive archetypes like $[Ca_2N]^{+}\cdot e^{-}$ and $[Gd_2C]^{2+}\cdot 2e^{-}$ cannot survive standard lithographic processing. This applies to applications such as Ohmic contacts to 2D semiconductors, room-temperature spintronic injectors, and low-work-function thin-film electrodes. Self-passivating chalcogenides such as Hf_2S and Ti_2S [21, 23] provide one route. Surface-functionalised 2D electrides do as well, including brominated Ca_2N [46, 48] and h-BN-encapsulated heterostructures. Air- and water-stable intermetallic electrides offer a particularly attractive alternative. They do not rely on passivation. Examples include Y_5Si_3 [19], ternary LaTMSi compounds where TM = Co, Fe, Mn, or Sc [24-26], and machine-learning-discovered A_2BC_2 phases [12]. Although their reported polycrystalline work functions (3.0–4.0 eV) sit slightly above clean C12A7:e^{-} or Ca_2N, they remain well below conventional refractory metals (W, Mo) while maintaining intrinsic metallic conduction and surviving ambient fabrication flows without growing a resistive oxide skin. Establishing clean-facet work functions, sputtered thin-film growth, and contact resistance benchmarks for these intermetallic electrides will be critical. So will executing the decisive glovebox-transfer contact test for 2D electrides on TMD transistors. Together, these steps will determine how broadly electrides expand from vacuum electron sources into mainstream solid-state nanoelectronics.

Availability of data and materials

Data sharing is not applicable to this article as no new datasets were generated during the current study.

Competing interests

The authors have no competing interests to declare that are relevant to the content of this article.

Funding

This research was funded by the Key Research and Development Program of Shaanxi Province (Grant No. 2025CY-YBXM-635), awarded to Kang Chen, and the Shenzhen Science and Technology Program (Grant No. JCYJ20230807145501003), awarded to Yutong Gong and Zhiqi Wang. The funding bodies had no role in the design of the study; in the collection, analysis, and interpretation of data; or in the writing of the manuscript.

Author contribution

Chenyang Zhao: Conceptualization, Investigation, Writing – original draft, Visualization. Kang Chen: Investigation, Data curation, Writing – review & editing. Qingyu Meng: Investigation, Writing – review & editing. Yelizaveta A. Morkhova and Yutong Gong: Writing – review & editing. Zhiqi Wang: Conceptualization, Supervision, Project administration, Writing – review & editing. All authors have read and agreed to the published version of the manuscript.

Acknowledgements

The authors also thank the copyright holders for permission to reproduce the figures included in this review. Specifically, Fig. 3(a), Fig. 3(b), Fig. 3(c), and Fig. 3(d) are reprinted with permission from refs. [38], [27], [47], and [42], respectively: © 2023 Elsevier Ltd.; © 2017 National Academy of Sciences; © 2008 American Chemical Society; and © 2008 Elsevier B.V. Permission for these reproductions has been obtained, and copies of the permission documentation are retained by the authors.

References

[1] Dye JL. Electrides: Ionic Salts with Electrons as the Anions. *Science* 1990, **247**: 663–668.

[2] Dye JL. Electrons as Anions. *Science* 2003, **301**: 607–608.

[3] Issa D, Dye JL. Synthesis of cesium 18-crown-6: the first single-crystal electride? *J Am Chem Soc* 1982, **104**: 3781–3782.

[4] Matsuishi S, Toda Y, Miyakawa M, *et al.* High-Density Electron Anions in a Nanoporous Single Crystal: $[Ca_{24}Al_{28}O_{64}]^{4+}(4e^{-})$. *Science* 2003, **301**: 626–629.

[5] Sushko PV, Shluger AL, Hayashi K, *et al.* Electron Localization and a Confined Electron Gas in Nanoporous Inorganic Electrides. *Phys Rev Lett* 2003, **91**: 126401.

[6] Hosono H, Kitano M. Advances in Materials and Applications of Inorganic Electrides. *Chem Rev* 2021, **121**: 3121–3185.

[7] Kim SW, Hosono H. Synthesis and properties of $12CaO{\cdot}7Al_2O_3$ electride: review of single crystal and thin film growth. *Philos Mag* 2012, **92**: 2596–2628.

[8] Inoshita T, Jeong S, Hamada N, *et al.* Exploration for Two-Dimensional Electrides via Database Screening and Ab Initio Calculation. *Phys Rev X* 2014, **4**: 031023.

[9] Tada T, Takemoto S, Matsuishi S, *et al.* High-Throughput ab Initio Screening for Two-Dimensional Electride Materials. *Inorg Chem* 2014, **53**: 10347–10358.

[10] Burton LA, Ricci F, Chen W, *et al.* High-Throughput Identification of Electrides from All Known Inorganic Materials. *Chem Mater* 2018, **30**: 7521–7526.

[11] Guo Z, Meng W, Zhang Q, *et al.* 3D Topological Inorganic Electrides: Screening, Properties, and Applications. *Adv Sci* 2025, **12**: e07469.

[12] Wang Z, Gong Y, Evans ML, *et al.* Machine Learning-Accelerated Discovery of A_2BC_2 Ternary Electrides with Diverse Anionic Electron Densities. *J Am Chem Soc* 2023, **145**: 26412–26424.

[13] Wang Z, Su J, Li C, *et al.* Electride-Induced Electronic Modulation of Ruthenium Catalyst for Highly Efficient Alkaline Hydrogen Evolution. *Adv Sci* 2026, **13**: e74939.

[14] Meng W, Bai J, Ma F, *et al.* Magnetic electrides: Recent advances in materials realization and application prospects. *Appl Phys Rev* 2025, **12**: 011320.

[15] Wang Y, Wang L, Gong Y, *et al.* Magnetic electrides: anion-engineered spin-topology phenomena. *J Mater Chem C* 2026, **14**: 487–498.

[16] Wang J, Hanzawa K, Hiramatsu H, *et al.* Exploration of Stable Strontium Phosphide-Based Electrides: Theoretical Structure Prediction and Experimental Validation. *J Am Chem Soc* 2017, **139**: 15668–15680.

[17] Lee K, Kim SW, Toda Y, *et al.* Dicalcium nitride as a two-dimensional electride with an anionic electron layer. *Nature* 2013, **494**: 336–340.

[18] Zhang X, Xiao Z, Lei H, *et al.* Two-Dimensional Transition-Metal Electride Y_2C. *Chem Mater* 2014, **26**: 6638–6643.

[19] Lu Y, Li J, Tada T, *et al.* Water Durable Electride Y_5Si_3: Electronic Structure and Catalytic Activity for Ammonia Synthesis. *J Am Chem Soc* 2016, **138**: 3970–3973.

[20] Zhang Y, Xiao Z, Kamiya T, *et al.* Electron Confinement in Channel Spaces for One-Dimensional Electride. *J Phys Chem Lett* 2015, **6**: 4966–4971.

[21] Ren S, Park KR, Regmi B, *et al.* Ultrastable One-Dimensional Ti_2S Electride Support for an Efficient and Durable Bifunctional Electrocatalyst. *Carbon Energy* 2025, **7**: e70070.

[22] Lee SY, Hwang JY, Park J, *et al.* Ferromagnetic quasi-atomic electrons in two-dimensional electride. *Nat Commun* 2020, **11**: 1526.

[23] Kang SH, Bang J, Chung K, *et al.* Water- and acid-stable self-passivated dihafnium sulfide electride and its persistent electrocatalytic reaction. *Sci Adv* 2020, **6**: eaba7416.

[24] Sun Y, Ma H, Jiao Y, *et al.* Water-Induced Structural Evolution of LaTMSi Ternary Intermetallic Electrides. *Chem Mater* 2023, **35**: 1972–1979.

[25] Gong Y, Li H, Wu J, *et al.* Unique Catalytic Mechanism for Ru-Loaded Ternary Intermetallic Electrides for Ammonia Synthesis. *J Am Chem Soc* 2022, **144**: 8683–8692.

[26] Wu J, Gong Y, Inoshita T, *et al.* Tiered Electron Anions in Multiple Voids of LaScSi and Their Applications to Ammonia Synthesis. *Adv Mater* 2017, **29**: 1700924.

[27] Hosono H, Kim J, Toda Y, *et al.* Transparent amorphous oxide semiconductors for organic electronics: Application to inverted OLEDs. *Proc Natl Acad Sci USA* 2017, **114**: 233–238.

[28] Toda Y, Yanagi H, Ikenaga E, *et al.* Work Function of a Room-Temperature, Stable Electride $[Ca_{24}Al_{28}O_{64}]^{4+}(e^{-})_4$. *Adv Mater* 2007, **19**: 3564–3569.

[29] Kim SW, Toda Y, Hayashi K, *et al.* Synthesis of a Room Temperature Stable $12CaO{\cdot}7Al_2O_3$ Electride from the Melt and Its Application as an Electron Field Emitter. *Chem Mater* 2006, **18**: 1938–1944.

[30] Druffel DL, Kuntz KL, Woomer AH, *et al.* Experimental Demonstration of an Electride as a 2D Material. *J Am Chem Soc* 2016, **138**: 16089–16094.

[31] Heiler A, Waetzig K, Tajmar M, *et al.* Work function performance of a C12A7 electride surface exposed to low pressure low temperature hydrogen plasmas. *J Vac Sci Technol A* 2020, **39**: 013002.

[32] Zou W, Khan K, Zhao X, *et al.* Direct fabrication of C12A7 electride target and room temperature deposition of thin films with low work function. *Mater Res Express* 2017, **4**: 036408.

[33] Nishio Y, Nomura K, Miyakawa M, *et al.* Fabrication and transport properties of $12CaO{\cdot}7Al_2O_3$ (C12A7) electride nanowire. *Phys Status Solidi A* 2008, **205**: 2047–2051.

[34] Toda Y, Matsuishi S, Hayashi K, *et al.* Field Emission of Electron Anions Clathrated in Subnanometer-Sized Cages in $[Ca_{24}Al_{28}O_{64}]^{4+}(4e^{-})$. *Adv Mater* 2004, **16**: 685–689.

[35] Toda Y, Kim SW, Hayashi K, *et al.* Intense thermal field electron emission from room-temperature stable electride. *Appl Phys Lett* 2005, **87**: 254103.

[36] Kottke NG, Waetzig K, Schilm J, *et al.* Improvement of the thermionic emission properties of C12A7 electride. *Vacuum* 2024, **227**: 113435.

[37] Rand LP, Williams JD. A Calcium Aluminate Electride Hollow Cathode. *IEEE Trans Plasma Sci* 2015, **43**: 190–194.

[38] Drobny C, Wätzig K, Rost A, *et al.* Endurance operation of a heaterless C12A7 electride plasma cathode and post operation material analysis. *Acta Astronaut* 2024, **214**: 231–239.

[39] Nakano H, Hoshino K, Ishikawa T, *et al.* Beam current enhancement of negative ion source on EVISS by pre-treating C12A7 electride. *J Phys Conf Ser* 2026, **3237**: 012062.

[40] Toledo J, Post A, Plaza JF. Measurement of the C12A7:e^- thermionic emission enhancement due to photon exposure. *J Phys Conf Ser* 2023, **2526**: 012111.

[41] Yanagi H, Kim KB, Koizumi I, *et al.* Low Threshold Voltage and Carrier Injection Properties of Inverted Organic Light-Emitting Diodes with $[Ca_{24}Al_{28}O_{64}]^{4+}(4e^-)$ Cathode and $Cu_{2-x}Se$ Anode. *J Phys Chem C* 2009, **113**: 18379–18384.

[42] Adachi Y, Kim SW, Kamiya T, *et al.* Bistable resistance switching in surface-oxidized C12A7:e^- single-crystal. *Mater Sci Eng B* 2009, **161**: 76–79.

[43] Yushkov ID, Kamaev GN, Volodin VA, *et al.* Resistance Switching in Polycrystalline C12A7 Electride. *Micromachines* 2022, **13**: 1917.

[44] Rybak AA, Yushkov ID, Nikolaev NA, *et al.* Electrophysical Properties of Polycrystalline C12A7:e^- Electride. *Electronics* 2022, **11**: 668.

[45] Wang X, Yu S, Xu Y, *et al.* Ohmic contacts of the two-dimensional Ca_2N/MoS_2 donor–acceptor heterostructure. *Phys Chem Chem Phys* 2023, **25**: 15433–15440.

[46] Tang W, Chen HY, Niu X. Tunneling-Barrier-Free Ohmic Contacts at 2D Electride/Semiconductor Interfaces. *ACS Nano* 2026, **20**: 16965–16975.

[47] Niu X, Niu Z, Shan W, *et al.* 2D Electron Gas-Induced the Lowered Tunneling Barrier and Ohmic Behavior Simultaneously in 2D Metal-Semiconductor Contacts. *Adv Funct Mater* 2026, **36**: e13567.

[48] Pan C, Sun D, Lin Z, *et al.* Coexistence of Ohmic Contact and Fermi Level Pinning at 2D Electride/2D Semiconductor Interfaces. *J Am Chem Soc* 2026, **148**: 1655–1661.

[49] Li D, Cheng Y, Cai M, *et al.* Uniform arrays of carbon nanotubes applied in the field emission devices. *Sci China Phys Mech Astron* 2013, **56**: 2081–2084.

[50] Goebel DM, Katz I. Ion and Hall Thruster Plumes. In: *Fundamentals of Electric Propulsion: Ion and Hall Thrusters*. Hoboken (NJ): John Wiley & Sons, 2008: 393–428.

[51] Hua Z, Wang P, Xu Z, *et al.* Experimental characterization of the C12A7 hollow cathode and its joint operation with a low-power Hall thruster. *Vacuum* 2021, **192**: 110443.

[52] McDonald MS, Caruso NRS. Ignition and Early Operating Characteristics of a Low-Current C12A7 Hollow Cathode. In: *35th International Electric Propulsion Conference (IEPC), Atlanta, GA, USA*. 2017: pp. 1–8; paper IEPC-2017-253.

[53] Sarver-Verhey TR. 28,000 Hour Xenon Hollow Cathode Life Test Results. In: *25th International Electric Propulsion Conference (IEPC)*. 1997: paper IEPC-97-168.

[54] Fantz U, Hopf C, Wünderlich D, *et al.* Towards powerful negative ion beams at the test facility ELISE for the ITER and DEMO NBI systems. *Nucl Fusion* 2017, **57**: 116007.

[55] Sun L, Yoshida T, Harada Y, *et al.* Amorphous dielectric metal-organic electron injection layer for efficient inverted organic light-emitting diodes. *Org Electron* 2023, **122**: 106878.

[56] Wong HSP, Lee HY, Yu S, *et al.* Metal–Oxide RRAM. *Proc IEEE* 2012, **100**: 1951–1970.

[57] Shen PC, Su C, Lin Y, *et al.* Ultralow contact resistance between semimetal and monolayer semiconductors. *Nature* 2021, **593**: 211–217.

[58] Li W, Gong X, Yu Z, *et al.* Approaching the quantum limit in two-dimensional semiconductor contacts. *Nature* 2023, **613**: 274–279.

[59] Ikeda S, Hayakawa J, Ashizawa Y, *et al.* Tunnel magnetoresistance of 604% at 300 K by suppression of Ta diffusion in CoFeB/MgO/CoFeB pseudo-spin-valves annealed at high temperature. *Appl Phys Lett* 2008, **93**: 082508.

[60] Huang RH, Dye JL. Low temperature (−80°C) thermionic electron emission from alkalides and electrides. *Chem Phys Lett* 1990, **166**: 133–136.

[61] Phillips RC, Pratt WP, Dye JL. Thermionic Emission from Cold Electride Films. *Chem Mater* 2000, **12**: 3642–3647.

[62] Kim KB, Kikuchi M, Miyakawa M, *et al.* Photoelectron Spectroscopic Study of C12A7:e^- and Alq3 Interface: The Formation of a Low Electron-Injection Barrier. *J Phys Chem C* 2007, **111**: 8403–8406.

[63] Yanagi H, Kuroda T, Kim KB, *et al.* Electron injection barriers between air-stable electride with low work function, C12A7:e^-, and pentacene, C_{60} and copper phthalocyanine. *J Mater Chem* 2012, **22**: 4278–4281.

[64] Yuan M, Quan LN, Comin R, *et al.* Perovskite energy funnels for efficient light-emitting diodes. *Nat Nanotechnol* 2016, **11**: 872–877.

[65] Dai X, Zhang Z, Jin Y, *et al.* Solution-processed, high-performance light-emitting diodes based on quantum dots. *Nature* 2014, **515**: 96–99.

[66] Stolterfoht M, Caprioglio P, Wolff CM, *et al.* The impact of energy alignment and interfacial recombination on the internal and external open-circuit voltage of perovskite solar cells. *Energy Environ Sci* 2019, **12**: 2778–2788.

[67] Boyd CC, Cheacharoen R, Leijtens T, *et al.* Understanding Degradation Mechanisms and Improving Stability of Perovskite Photovoltaics. *Chem Rev* 2018, **119**: 3418–3451.

[68] Hosono H, Kim SW, Miyakawa M, *et al.* Thin film and bulk fabrication of room-temperature-stable electride C12A7:e^- utilizing reduced amorphous $12CaO{\cdot}7Al_2O_3$ (C12A7). *J Non-Cryst Solids* 2008, **354**: 2772–2776.

[69] Hirayama M, Matsuishi S, Hosono H, *et al.* Electrides as a New Platform of Topological Materials. *Phys Rev X* 2018, **8**: 031067.

[70] Hosono H, Hayashi K, Kajihara K, *et al.* Oxygen ion conduction in $12CaO{\cdot}7Al_2O_3$: O^{2-} conduction mechanism and possibility of O^- fast conduction. *Solid State Ionics* 2009, **180**: 550–555.

[71] Miyakawa M, Kim SW, Hirano M, *et al.* Superconductivity in an Inorganic Electride $12CaO{\cdot}7Al_2O_3$:e^-. *J Am Chem Soc* 2007, **129**: 7270–7271.

[72] Tanaka S, Kato T, Miyake A, *et al.* Strong enhancement of superconductivity in inorganic electride $12CaO{\cdot}7Al_2O_3{:}e^-$ under high pressure. *J Korean Phys Soc* 2013, **63**: 477–480.

[73] Williams J, Akinc M. Processing and Oxidation Behavior of Y5Si3. In: *Proceedings of the 21st Annual Conference on Composites, Advanced Ceramics, Materials, and Structures—A: Ceramic Engineering and Science Proceedings*. Singh JP, Ed. Westerville (OH): American Ceramic Society, 1997; 18(3A): 571–578. DOI: 10.1002/9780470294437.ch62.

Author biography



Chenyang Zhao, a sophomore undergraduate student majoring in Communication Engineering at the School of Telecommunications Engineering, Xidian University. He has mastered theories related to digital systems and basic circuits.



Zhiqi Wang received his B.S. and M.S. degrees from Northwestern Polytechnical University (NWPU), Xi'an, China. He is currently a Ph.D. candidate at NWPU. His current research interests mainly focus on the intelligent design of electron-rich materials and their applications in energy-related fields.

Graphical abstract

